Experimental and numerical study of gas-powder flux in coaxial laser cladding nozzles of Precitec

M. Doubenskaia, Aleksandr Kulish, Alexey Sova, P. Petrovskiy, I. Smurov

Version of Record: https://www.sciencedirect.com/science/article/pii/S0257897220313426
Manuscript_9734fd79feba41e6ff3063e99b2fe359

Experimental and numerical study of gas-powder flux in coaxial laser cladding nozzles of Precitec

M. Doubenskaia[1*], A. Kulish[1], A. Sova[1], P. Petrovskiy[2], I. Smurov[1, 2]

[1] Lyon University, ENISE, LTDS Laboratory, UMR CNRS 5513, 58 rue Jean Parot, 42023 Saint-Etienne Cedex 2, France

[2] National University of Science and Technology "MISiS", 4 Leninsky prospect, 119991 Moscow, Russia

Keywords: coaxial laser cladding, gas-powder flux modelling, process monitoring, cladding nozzle geometry.

Abstract: Laser cladding technology is used for coating deposition, worn surfaces repairing, and direct fabrication. However, the technological complexity and high cost prevents its wide industrial applications. In the present work, the gas-powder flux parameters are studding to optimise cladding conditions and the choice of appropriate nozzle. Using commercial Precitec (Germany) nozzles, the relations between the nozzle geometry and the powder flux parameters are analysed. The numerical simulation of gas and powder flux is compared with high-speed optical monitoring accompanied by post image treatment. Numerical simulation and experimental results have the same tendencies regarding the powder flux geometry, waist parameters and convergence angles. The difference is related to particle-particle collisions, which are neglected in simulation. The modelling results strongly depend on the energy loses in particle/nozzle wall collisions. It was found that for industrial cladding "short" nozzles with high-gap are more suitable. For 3D direct fabrication, the "medium" nozzles with low-gap are preferable.

---

*maria.doubenskaia@enise.fr; phone : +33(0)477437565 ; fax : +33(0)477743497

1. Introduction

Laser cladding is one of the perspective and demanded technologies. By coaxial powder injection, it is possible to deposit protective coatings, repair worn surfaces or even perform a 3D direct fabrication. Despite several advantages over traditional spraying techniques, in particular metallurgical contact with substrate, laser cladding is still challenging and high cost [1]. A number of process parameters should be optimised. Particularly, it concerns powder flow problem, which is one of the important factors defining the geometry and quality of cladding layers. Therefore, it is necessary to study this field theoretically and experimentally including optimization of laser cladding nozzles, modelling of powder transport phenomena, application of different monitoring techniques, etc. [2-4].

Numerous efforts were applied to different study fields noted above. Whereas researchers proposed new nozzle designs to improve powder catchment efficiency [5-7], some of them investigated and optimized the existing ones. Based on the modelling results, Yan [6] determined and manufactured the optimal coaxial nozzle with suitable parameters for laser cladding regarding its high powder catchment and laser efficiency. In order to reduce the powder divergence, spot size and increase efficiency, 3D novel model was applied by Ju et al. [8].

Large group of investigations was dedicated to numerical [9] and analytical [10] study of gas-powder phenomena. The last one is versatile and reliable approximation instrument, however, depending on experimental results [11]. The most crucial and powerful field here is numerical modelling based on computational fluid dynamics (CFD). Starting from relatively simple models served to find powder concentration field assuming particles path and speed [12], researchers tried to implement more complicated models. These models included particle-particle and particle-wall interactions [13, 14], laser beam attenuation and particle preheating [15, 16], interactions near substrate [17] etc. Moreover, 3D models appeared within last few years, which are able to predict and explain numerous physical phenomena

and resolve assumptions normally proposed before. Despite the considerable time needed for simulation, several researchers are already applied them to study various problems including even solidification and convection of liquid metal. For example, Khamidullin et al. [18] studied the influence of technological parameters and powder properties on laser cladding performance. Zhang et al. [19] used 3D numerical modelling results to evaluate a novel coaxial nozzle and to find optimal cladding parameters.

Particle-in-flight monitoring procedure is useful for cladding optimization by reducing experimental efforts. Among simple and popular methods of optical diagnostic one may note application of different cameras: CCD camera was used to observe powder flow and to study the influence of gas flow on particles velocity [20-24]. Tan et al. [25] using images acquired by a high-speed camera defined powder flow density and particle-in-flight speed. For powder flow long-term observation Tan et al. [26] used high-speed camera and line laser diode for more accurate measurements. Several researchers tried to add additional mirrors to visualise the flow from the side [27], powder weight measurements using containers of different diameter [28] and substrate with pinhole and high-precision balance [17].

Despite of considerable number of papers analysing gas-powder flow problem, the comprehensive studies of cladding nozzle optimization are still not numerous. In particular, it concerns the study of commercial nozzles with different gap width, coincidence angle and, as follows; the nozzle choice for a specific technological objective: repairing, direct fabrication, etc. There is limited practical information concerning particle-in-flight for commercial nozzles widely applied in industrial laser cladding.

The present paper contributes to the solution of this problem employing a set of industrial, commercial coaxial nozzles fabricated by Precitec (Germany). They are known by correct performance to cost ratio. By changing the nozzle's gap width and coincidence angle, the differences and particularities of gas-powder flows were examined. However, prior to

experimental study of gas-powder flux a numerical analysis was performed to predict its parameters as velocity field, particles trajectories, their concentration, etc.

Particular attention was applied for the analysis of nozzle geometry, which defines the conditions of gas and powder injection, on particles jet geometry.

2. Numerical simulation of gas-powder flow

Laser cladding problem includes two particular cases for consideration namely the carrier and shielding gases flows and particles motion inside this flow. Eulerian - Lagrangian Model is applied, several authors recommend this method specifically for the laser cladding technology [28, 29].

2.1 Gas flow governing equations

The set of Navier – Stokes equations is solved for the fluid phase (carrier or shield gas). Assuming a compressible fluid, for example, carrier gas, one need to consider a Reynolds-Averaged Navier-Stokes (RANS) formulation, which averages the velocity and pressure fields in time due to the turbulent nature of gas-powder flows. Particularly, the turbulent viscosity is evaluated using turbulence models. The most common one is the $k-\varepsilon$ turbulence model. It consists of solving two additional equations for the transport of turbulent kinetic energy k and turbulent dissipation ε. The exact $k-\varepsilon$ equations contain many unknown and unmeasurable terms, but the more applicable forms with minimum unknowns are shown below [28].

For the turbulent kinetic energy k:

$$\frac{\partial(\rho k u_i)}{\partial x_i} = \frac{\partial}{\partial x_j}\left[(\mu + \frac{\mu_T}{\sigma_k})\frac{\partial k}{\partial x_j}\right] + G_k + G_b - \rho\varepsilon, \quad (1)$$

For the turbulent energy dissipation ε:

$$\frac{\partial(\rho\varepsilon u_i)}{\partial x_i} = \frac{\partial}{\partial x_j}\left[(\mu + \frac{\mu_T}{\sigma_k})\frac{\partial \varepsilon}{\partial x_j}\right] + \frac{C_{1\varepsilon}\varepsilon}{k}(G_k + G_b) - C_{2\varepsilon}\rho\varepsilon\frac{\varepsilon^2}{k}, \quad (2)$$

$$\mu_T = \rho C_\mu {k^2}/{\varepsilon}, \quad (3)$$

$$G_k = \mu_T({\partial u_j}/{\partial x_i} + {\partial u_i}/{\partial x_j})\,{\partial u_i}/{\partial x_j}, \quad (4)$$

$$G_b = -g_i({\mu_T}/{\rho Pr_t}\,{\partial \rho}/{\partial x_i}), \quad (5)$$

In the abovementioned equations ρ is the density, u_i is the velocity, x_i is the position, E_{ij} is a component of rate of deformation, μ_T is an eddy (turbulent) viscosity, Pr_t is the turbulent Prandtl number, g_i is the gravitational acceleration, G_k is the generation of turbulence kinetic energy due to the velocity gradients, and G_b is due to buoyancy. $C_\mu = 0{,}09, \sigma_k = 1, \sigma_\varepsilon = 1.3$, $C_{1\varepsilon} = 1.44, C_{2\varepsilon} = 1.92$ are the empirical constants obtained by numerical iterations for any turbulent flow.

2.2 Powder flux modelling

The dispersed phase flow problem basically stands for obtaining each particle trajectory by solving typical Newton's second law of mechanics [30] where m_p or V_p is a particle's mass and volume, a_p is an acceleration and $\sum_i F_i$ is a sum of all acting forces, u_p is the velocity, t is the time and $\vec{x}$ is the position vector.

$$\sum_i F_i = m_p a_p = \rho V_p\,{du_p}/{dt} = \rho V_p\,{d^2\vec{x}}/{dt^2}, \quad (6)$$

While particle moves along with carrier gas through the nozzle channel towards the substrate it is subjected mainly to gravity and drag forces. Since the powder flow generally is not laminar a well suitable drag force description is the Haider – Levenspiel model which

takes into account the particles' shape factor. It is known that, the main difference between all turbulent drag force models is related to drag coefficient, C_D, which is included in a general drag force equation where u_p is a particle velocity, u is the fluid phase velocity, d_p is diameter and R_e is the Reynolds number [28].

$$F_D = {18\mu C_D R_e}\Big/{24\rho {d_p}^2} \cdot (u - u_p), \tag{7}$$

According to the Haider – Levenspiel model the drag coefficient C_D can be presented like shown below.

$$C_D = {24}/{R_e}\left(1 + a_1 R_e^{a_2}\right) + {a_3 R_e}/{a_4 + R_e}, \tag{8}$$

With coefficients a_{1-4} written as follows [25]:

$$a_1 = \exp(2.3288 - 6.4581\varphi + 2.4486\varphi^2), \tag{9}$$

$$a_2 = 0.0964 + 0.5565\varphi, \tag{10}$$

$$a_3 = \exp(4.905 - 13.8944\varphi + 18.4222\varphi^2 - 10.2599\varphi^3), \tag{11}$$

$$a_4 = \exp(1.4681 + 12.2584\varphi - 20.7322\varphi^2 + 15.8855\varphi^3), \tag{12}$$

Where shape factor $\varphi = s \,/\, S$ takes into account how spherical a particle is. Basically, s is a surface area of a sphere having the same volume as a particle and S is an actual surface area of the particle.

2.3 Model adjustment for laser cladding

For laser cladding modelling the assumptions are as follows:

- fluid phase (gas) is viscous, compressible (Mach number $M < 0.3$) and thermally-conductive;

- substrate and dispersed phase materials are homogenous and solid;
- spherical powder particles with diameter 50 - 110 μm are concerned;
- particles interact with nozzle walls elastically or nonelastically but not mutually;
- the particles concentration in gas flow is low, so their influence on its parameters is negligible.

The calculation procedure was realized by Comsol software and the stated problem was solved within an axisymmetric frame. The initial conditions at $t = 0$ are set up according to parameters of an environment namely the initial pressure $P = P_0 = 1\ \text{atm} = 0.1\ \text{MPa}$, temperature $T = T_0 = 300\text{K}$ and initial velocity $u_0 = 0$. The computational domain is filled with Argon (Ar) which is also used for shield/carrier gas with feed rate of 5 and 9 l/min respectively. The boundary condition between gas and nozzle wall was set up so that gas velocity vector equals zero and boundary itself is thermally isolated.

Considering particles flux modelling, the particle-wall interaction is considered as elastic or inelastic depending on the coefficient of energy loses, α, which depends on particles shape, walls roughness, etc. It is proposed to use 0.7; 0.9; 1.0 as the values of α.

3. Experimental setup

3.1.Laser cladding equipment and powder properties

For the cladding set-up the TRUMPF Lasma 1054 (Germany) workstation was used with YC52 Precitec (Germany) cladding laser head allowing the application of different coaxial nozzles which can be separated into 3 groups: “long”, “medium” and “short”. The present experiments were carried out for “medium” and “short” nozzles. Their geometry is presented in Figure 1 and Table 1.

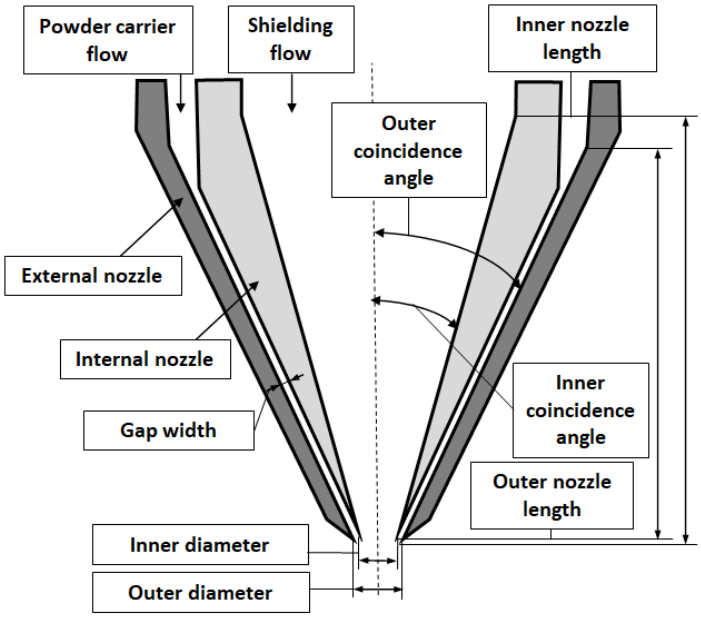

Fig. 1. Geometry of Precitec coaxial laser cladding nozzle.

Gap width is the width between inner and outer nozzles serving as the channel for powder injection. These nozzles have the possibility of changing the gap width between 0.5 and 1.0 mm as well as outlet diameter and coincidence angle. The geometric parameters for short and medium nozzles are presented in the Table1.

Tab. 1. Geometric parameters of the Precitec nozzles.

Nozzle type	Outer diameter, mm	Inner diameter, mm	Outer / Inner coincidence angle	Gap width, mm
Short	14 or 15	13	32°	0.5 or 1
Medium	11 or 12	10	25°	0.5 or 1

The powder feeder Sultzer Metco was used. It has two hoppers, a disk type of powder feeding system and embedded additional mixers with the maximum value of gas supply of 9

l/min and maximum rotating speed 90 rpm. The process parameters including gas/powder feed rates and powder material properties are presented in Table 2.

Table 2. Process parameters and powder properties for experiment and modelling.

Type of metal powder/supplier	Particle shape	Gas feed rate, (l/min)	Powder feed rate, (g/min)	Density, (kg/m^3)	Particle diameter range, (µm)
Inconel 718 / TLS Technik	Quasi-spherical	9	18	8190	50 - 110

The powder SEM image and particle size distribution are shown in Figure 2a and Figure 2b respectively.

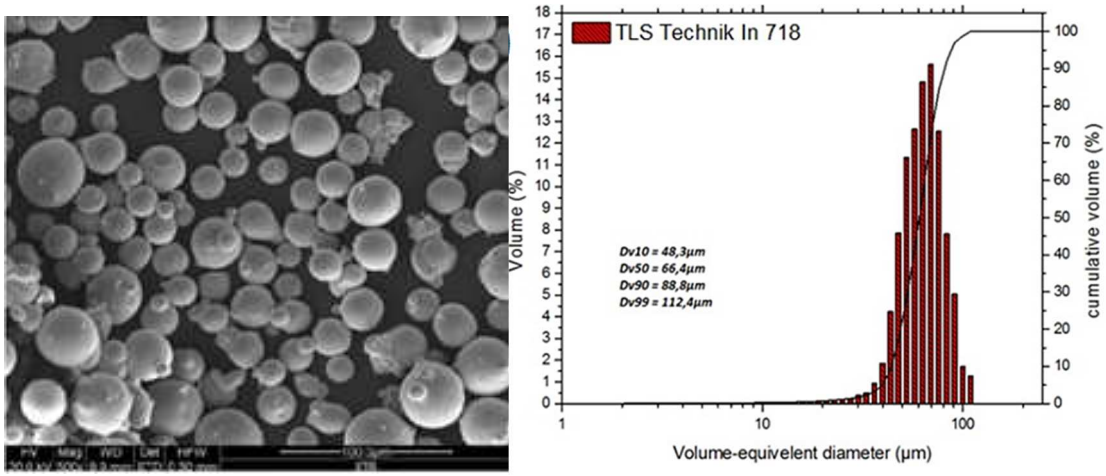

(a) (b)

Fig. 2. SEM image (a) and particle size distribution (b) of the Inconel 718 powder.

3.2.High-Speed camera

Powder flux monitoring was carried out by the Phantom VEO - 710L high-speed camera. The VEO 710 model has a one-megapixel CMOS sensor which is able to record up to 7400 fps at its full 1280 x 800 pixels resolution. For the illumination, four continuous light sources

were placed on shafts from the different sides to be on the same height with the nozzle (Figure 3). These light sources consisted of diode lamps MultiLED LT (GSVITEC, Germany) and diodes projection system in near-field (EFFISHARP, France). In the experiments the optical monitoring system operating at 100 frames per second (fps) was used.

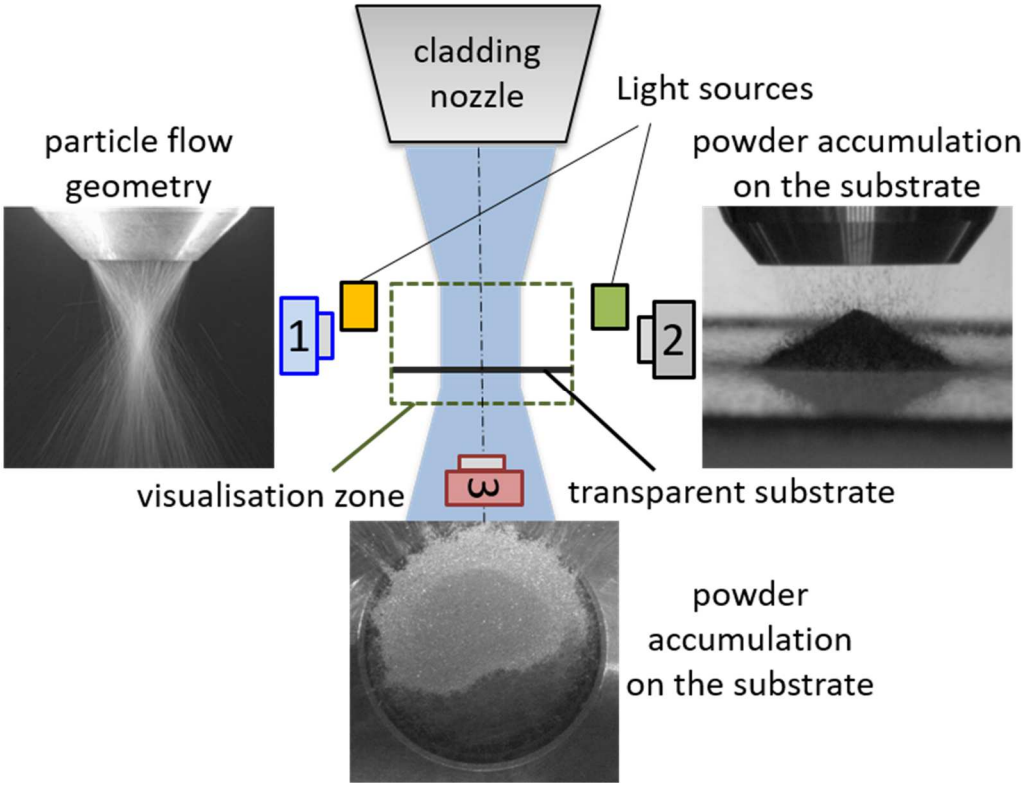

Fig 3. Experimental set-up.

To analyse the particles flux geometry the camera was installed perpendicular to the jet axis (Figure 3, position 1); to visualise powder deposition on the glass substrate it was oriented coaxially to the jet (Figure 3, position 3).

4. Results and Discussion

4.1 Modelling results

The gas flow underneath the nozzle is affected by the two interacting flows transporting powder particles and protecting laser head's optics (Figure 1). The external gas flow shapes the central one forming practically a one-dimensional coaxial flow. It can be seen on the gas flow velocity contours presented for the "short" and "medium" nozzles in the Figure 4a and Figure 4b. This is the typical solution used in another coaxial cladding heads with two internal and one external nozzles to shape the powder flux [31, 32].

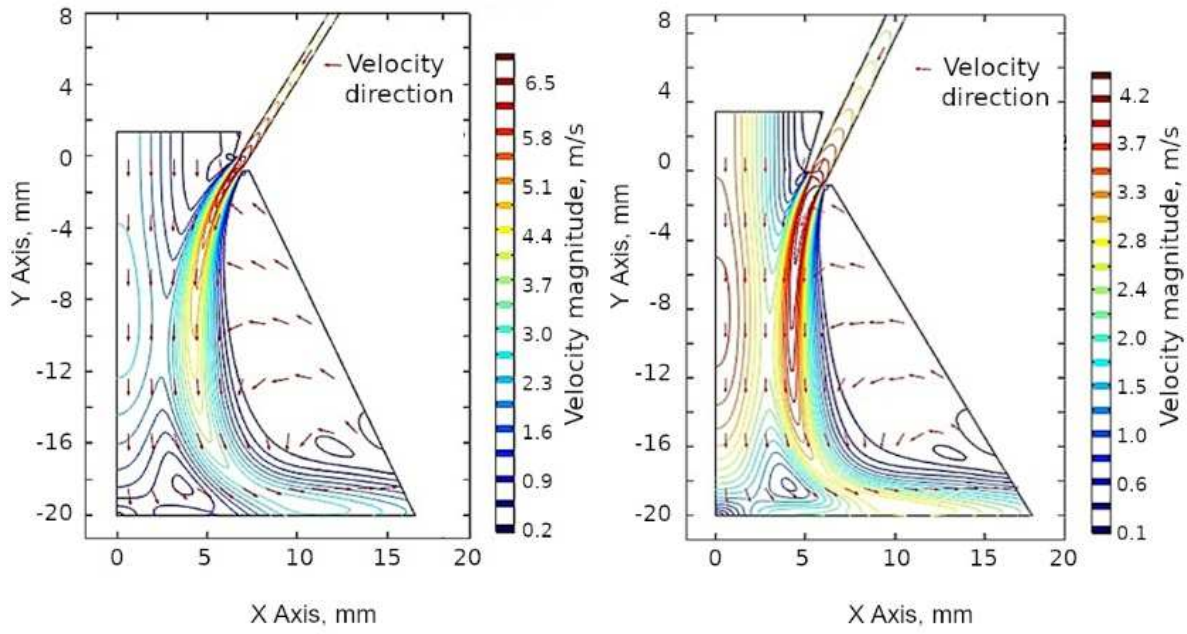

(a) (b)

Fig. 4. Gas velocity field for the "short" nozzle with 0.5mm gap (a) and the "medium" nozzle with 1.0 mm gap (b).

The Ar gas flowing out of the nozzle interacts with ambient gas and creates a toroidal-shaped vortex. Generally, the velocity fields have the similar structure but for the short and medium nozzles with the gap of 0.5 mm the mean gas velocity has its maximum value around 7 and 9 m/s respectively. For the 1mm gap nozzles with identical Ar gas feeding rate the corresponding velocity values are 3.5 and 4.5 m/s. The highest gas velocity results in the highest particle velocity so one may expect the fast particles for the 0.5 mm gap nozzles.

The gas flow velocities shown before are used to solve another problem: influence of the coefficient of energy loses, α, in collisions of particles with nozzle walls. It is not clear which value of α is the appropriate one for the applied powder and nozzle. In general, the energy losses in collisions of particles with walls depend on many parameters: the carrying gas velocity, concentration and inertial properties of the particles, channel geometry, irregularities on particles and wall roughness, etc. [33]. In recent papers the value of alfa is varied in between 0.7 [14] and 1.0 [34], often the value of 0.9 is applied. In the present paper the value of $\alpha = 0.9$ was chosen but several simulation results were obtained also for $\alpha = 1.0$ and $\alpha = 0.7$ values. The $\alpha = 1.0$ means that there is no energy loses whereas $\alpha = 0.7$ represents 30% of loses**.** The particles size and velocity distributions along the jet are shown in the Figure 5a, b for "short" nozzle and Figure 5c, d for the "medium" one.

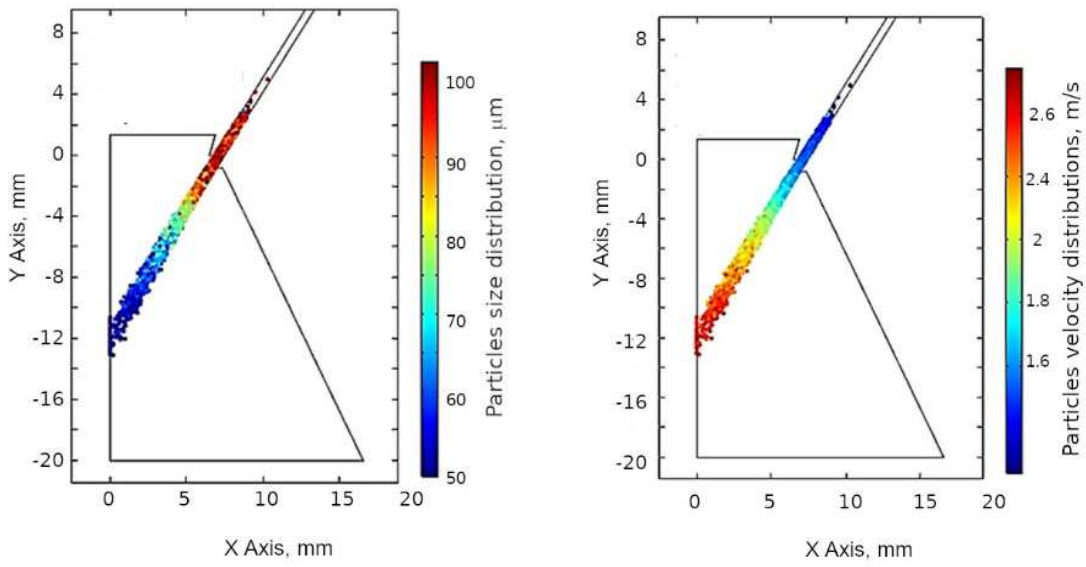

(a) (b)

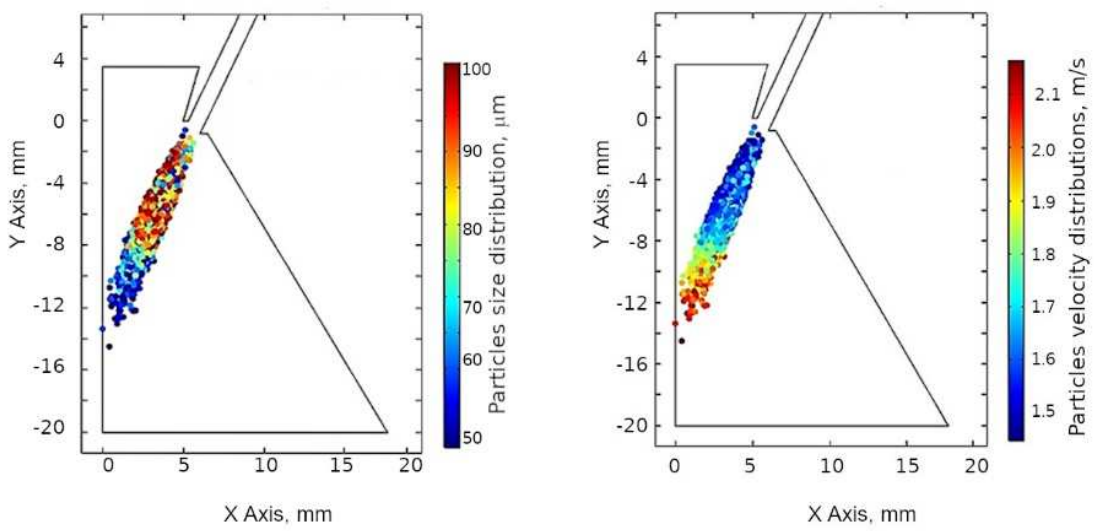

(c) (d)

Fig. 5. Particle size and velocities distribution along the jet: (a), (b) - "short" nozzle with 0.5mm gap; (c), (d) - "medium" nozzle with 1mm gap, coefficient of energy loses α is 0.9.

For the fixed value of the energy loses coefficient, α, but for different nozzle geometry, the number of particle/wall collisions is different, as well as the particle trajectory. That is why the results presented in Figure 5 (a, b) and (c, d) are different. The eventual variation of α value with nozzle geometry is the subject of additional study that is outside the scope of the present paper. Note that the variation of the coincidence angle for the results presented in Figure 5 is only 7° that is not large and probably does not influence too strong the α value.

For the low-gap nozzles particles are distributed without any mixing and their velocity is almost two times lower than the gas velocity: between 1.6 - 2.8 m/s and 1.4 - 1.8 m/s for low and high-gap nozzles respectively. For "medium" nozzles these values are 2.2 - 3.4 m/s and 1.5 - 2.2 m/s correspondingly. ~~The light particles having the maximum speed are moving in front of the others.~~ However, for high-gap nozzles particle flux represents a mixture between particles of different size. For "medium" nozzles the mixing of powder-in-flight is visible. This behavior may be explained by the high number of particle-wall collisions within a low-

gap channel leading to a significant energy loses. Moreover, particles with different mass and velocity interacts differently with the carrier gas.

The energy loses coefficient, α, drastically influences the powder flux as shown in Figure 6a, b. Without any energy loses particles form a widest range of trajectories which depends on the gap value. This phenomenon is similar for both types of nozzles. By reducing the loses coefficient, α, the range of particles trajectories is decreased significantly and, as a consequence, the particle density is increased. The position of that stream along vertical axis Y is almost the same for each coefficient α so the difference only with a number of lesser streams.

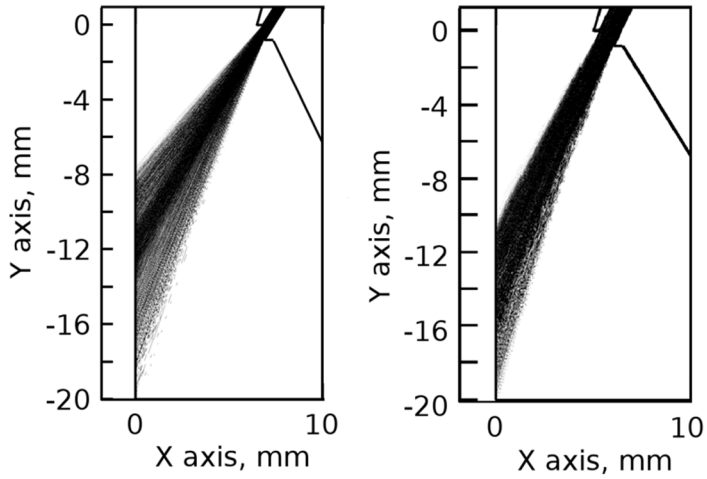

(a) (b)

Fig.6. The range of particles trajectories for the "short" nozzle with 0.5mm gap, α = 1.0 (a), and the "medium" one with 1 mm gap, α = 0.9 (b).

4.2 Comparison with the experimental results

Gas-powder jet images were obtained by the high-speed camera (see chapter 3) at 100 fps which corresponds to 9.9 ms of exposure time. Each physical value used in further analysis was defined based on averaging of 20 measurements. Being repetitively reflected from the walls, the particles may fly out from the nozzle within a wide range of directions defining the

convergence angle. At a certain point the powder flow is converged and along short distance forms the waist zone with almost equal width. This zone may be defined as the zone with highest powder density and for cladding required narrow bead width the deposition zone must be positioned within this area [32].

The post-treatment of optical image is necessary to measure the geometry of flow's waist and its position, particles concentration, etc. This post-treatment was realized using PCC 2.8 software varying image parameters such as gamma, gain and sensitivity. One of the post-treated images is shown in the Figure 7a as well as the flow scheme in the Figure 7b with certain geometrical parameters to be measured and compared with modelling results: d – waist diameter; l – waist lenght; L – waist position; θ_{convm}– the main convergence angle; $\theta_{conv1}$and θ_{conv2}– the limit convergence angles. The flow divergence and convergence angles are supposed to be equal to one another ($\theta_{divl} \approx \theta_{conv1}$).

For dense particles flux with their multiple collisions in the waist zone, the divergence angle would be larger than the convergence one. One can separate the total flow into the "main" and "secondary" streams (Figure 7a). The first one can be seen in the Figure 7a as the "blue zone" characterized by the dense powder flux with relatively light and dark zones. The maximum convergence angle, θ_{convm}, (Figure 7b) is formed between particles trajectories shown in the Figure 7a (the "blue zone") and the vertical axis Y. The "secondary" stream consists of the particles flowing outside of the "main" stream with less regular trajectories and lower density (Figure 7a, the "rose zone"). The particles belonging to the "secondary" stream form the limit angles ($\theta_{conv1}$and θ_{conv2} (Figure 7b)).

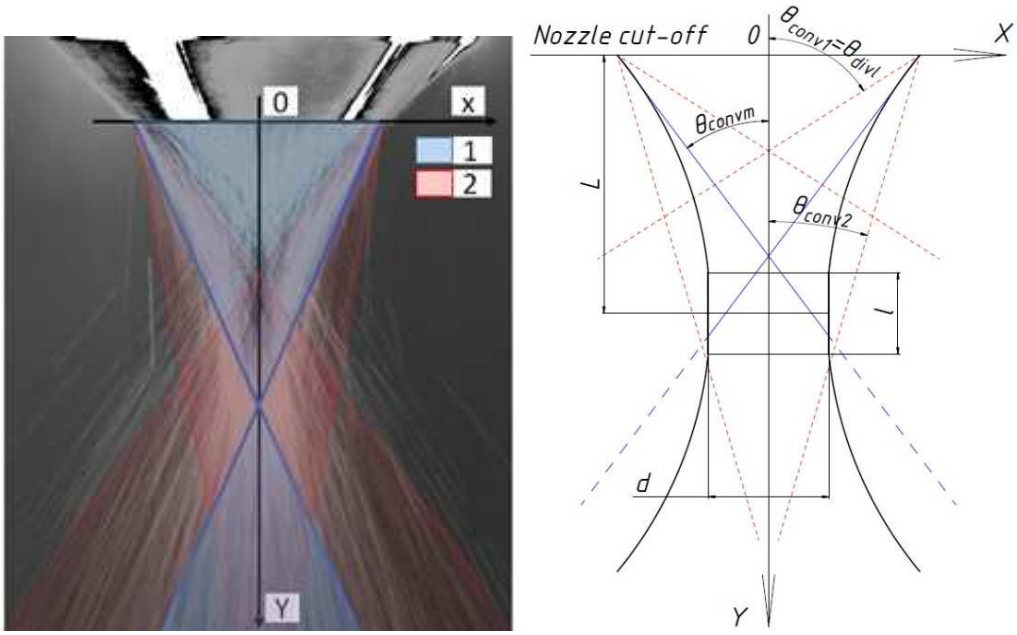

(a) (b)

Fig. 7. (a) - General view of gas-powder flow by optical monitoring: *1* – "main" stream; 2- "secondary" stream. (b) - Scheme of gas-powder flow with geometrical parameters.

Images of particle flux for the "middle" and "short" nozzles with 0.5 mm gap are recorded by high-speed camera and presented in Figure 8. The experimental results are limited by the red line, the simulation ones (for coefficient α = 1.0) – by the blue line. The superposition of experimental and simulation results are used for the convergence angles comparison.

In the simulation results the variation of the waist zone position with coefficient α is not significant, that is why the value of α =1.0 was chosen for further analysis.

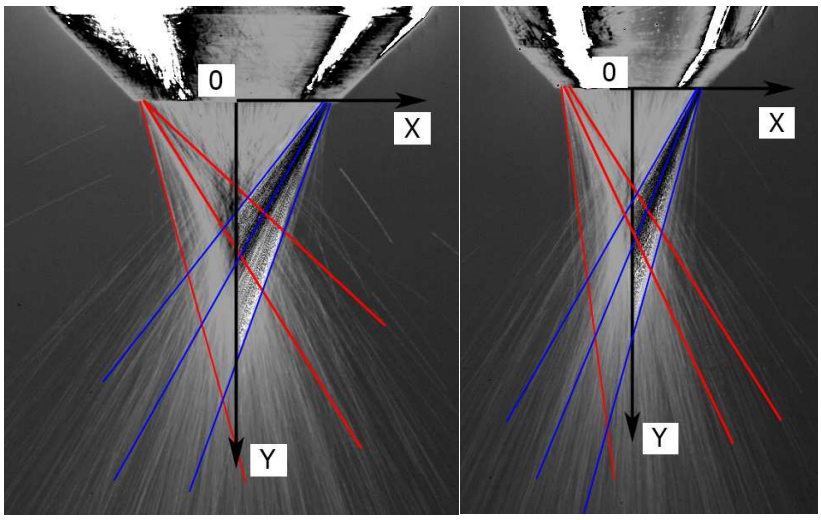

(a) (b)

Fig 8. Comparison of the experimental results with the computational ones: the "short" nozzle (a) and the "medium" one, (b); gap width is 0.5 mm, $\alpha = 1$. Blue lines correspond to simulation; the red ones to experiments.

Comparison of experimental and simulation results for the main convergence angles and limit angles is presented in Table 3.

The main convergence angles have close values for both simulation and experimental results, that is not clear, in particular keeping in mind that real value of α coefficient is less than 1.0 (used in simulation). This could be explained by the difficulties to measure the convergence angles from the post-treated images. That is why the obtained experimental results should be considered as the approximate ones. In any case the particles flux geometry based on simulation is narrower than the experimental one. The limit angles are typically larger in the case of measured powder flows even if compared with those from simulation using $\alpha = 1.0$. This is explained by the absence of particle-particle collisions in the model.

For the 1.0 mm gap width limit convergence angle could be closer to 0 degrees, that is practically parallel to the Y - axis. The particles from "secondary" stream are not integrated into the molten pool and decrease the deposition efficiency. The main convergence angle is

less for the “medium” nozzles compared with the “short” ones. The larger gap the nozzle has, the wider is the distribution of trajectories of the secondary and the “main” stream particles at the nozzle cut-off.

Table 3. Comparison of experimental and simulation results for the main convergence angles and limit angles.

Nozzle type/ gap width, mm	Experiment: convergence angles, ° ($\theta_{convm}/\theta_{conv1}$ and θ_{conv2})	Simulation: convergence angles, ° ($\theta_{convm}/\theta_{conv1}$ and θ_{conv2})
Short, 0.5 mm	32 ± 0.7 / 21 ± 0.5 and 38 ± 0.5	32 / 14 and 45
Short, 1.0 mm	32 ± 1.6 / 10 ± 0.5 and 40 ± 0.5	32 / 19 and 35
Medium, 0.5 mm	26 ± 1.1 / 9 ± 0.5 and 32 ± 0.5	25.5 / 15 and 30
Medium, 1.0 mm	22 ± 1.7 / 5 ± 0.5 and 30 ± 0.5	20.5 / 14 and 34

The light zone in the Figure 9a and b indicates the maximum of measured powder density for the “short” and “medium” nozzles with the 0.5 mm gap. The “short” nozzle with the 0.5 mm gap performs the densest powder flow at 8.6 mm from the nozzle cut-off Figure 9a; whereas for the high gap value this distance equals to 9.3 mm. The same tendency is observed when considering the “medium” type nozzles. Generally, the low-gap nozzles perform densest powder flux and better powder jet focalization. The standoff distance recommended by Precitec, that is the distance between the cladding nozzle and the workpiece, is equal to 10.5 - 11.5 mm for the “short” nozzles and to 11.5 - 12.5 mm for the “medium” ones [31].

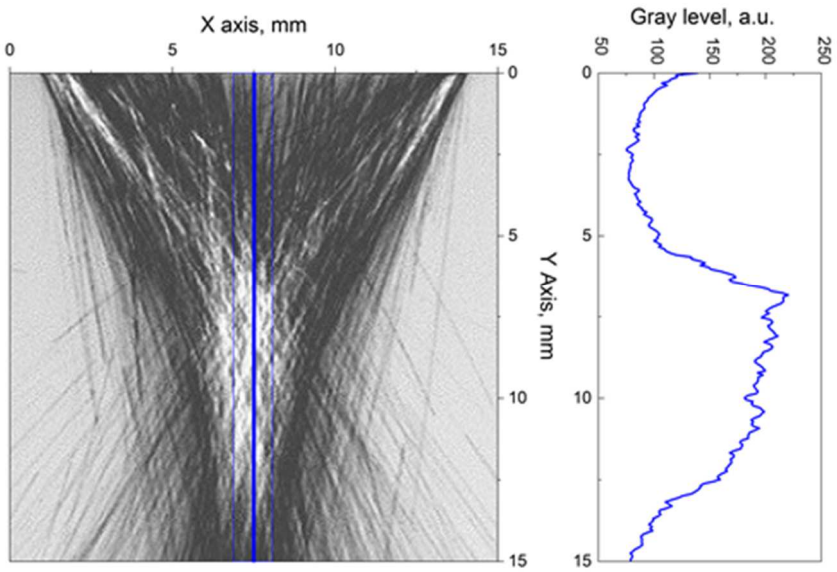

(a)

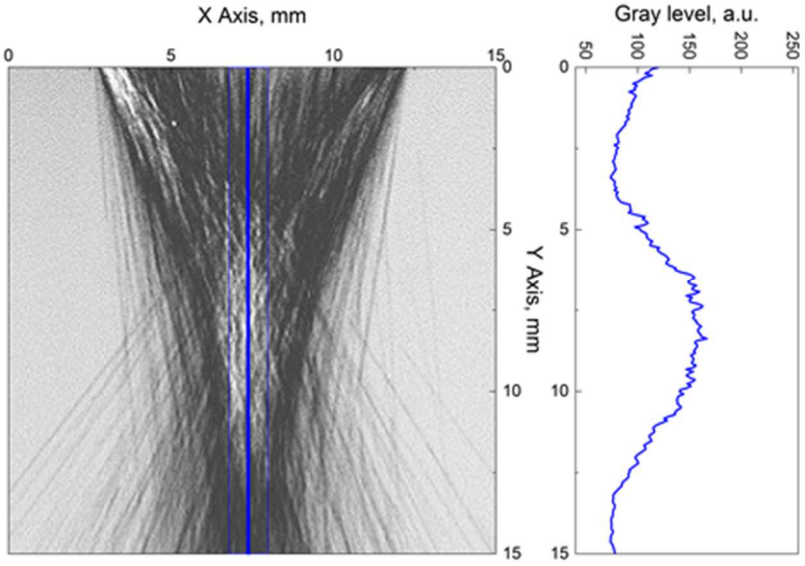

(b)

Fig. 9. Optical images of powder jet: general view and longitudinal profiles for the “short” (a) and the “medium” (b) nozzles. Gap width is 0.5 mm.

When comparing the simulation results with the experimental ones regarding the powder density and position of its maximum, the density profiles along *Y* axis obtained by Comsol can be directly superposed with the treated jet images as in Figure 9 for different energy loses coefficient α (Figure 10).

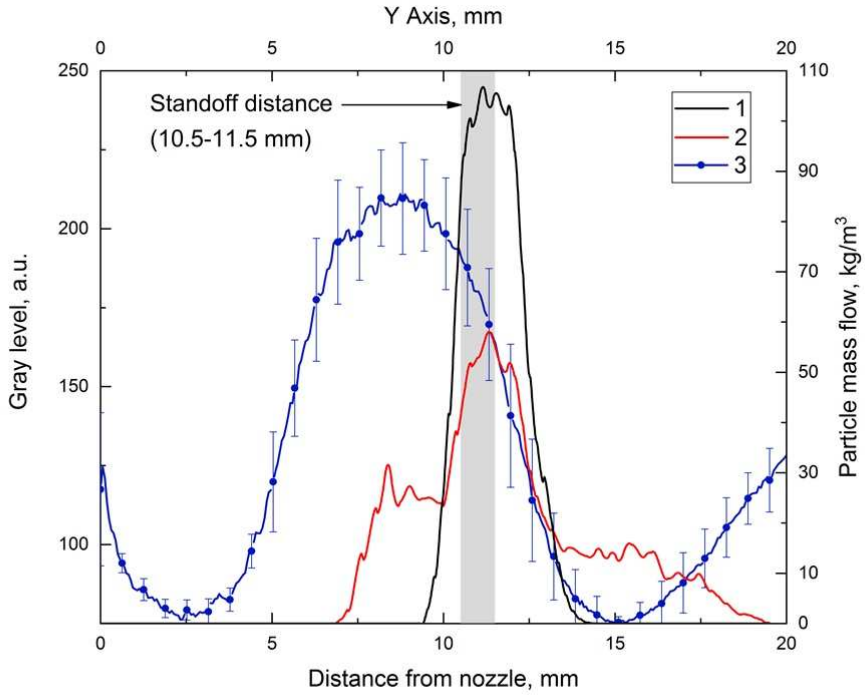

Fig. 10. Comparison of the powder jet density obtained by the simulation with the experimental one for the "short" nozzle, gap is 0.5mm. (1) – simulation with $\alpha = 1.0$ value; (2) - simulation with $\alpha = 0.9$ value; (3) – experimental results.

The curve *3* in Figure 10 represents the experimentally measured longitudinal profile of powder density whereas the curves *1* and *2* represent the density distribution obtained by the simulation for $\alpha = 1.0$ and $\alpha = 0.9$, respectively. Based on the results presented in Figures 8 and 10, it is possible to note the difference between experimental and simulation results for main convergence angles.

The waist position measured experimentally is closer to the nozzle than the calculated one. This distance increases from 8.6 to 9.3 mm with gap for « short » nozzles and from 8.3 to 9.1 mm for « medium » nozzles. Probably the difference is related to the particle-particle collisions (neglected in simulation) that are started before (8-9 mm) the formation of waist (12-14 mm). The corresponding values provided by Precitec are closer to the simulation results than the experimental ones [31].

The difference between convergence angles presented in Table 3 results in the difference between the powder flow waist positions L and the width d (fig. 7b).

The waist width d was studied experimentally (Figure 11b). To obtain such an image the additional post-treatment was carried out by varying the parameters like gain and sensitivity in the PCC software. For the gap equals 0.5 mm and "short" nozzle d = 4,1 ± 0,3 mm; for the "middle" nozzle d = 3,3 ± 0,3 mm.

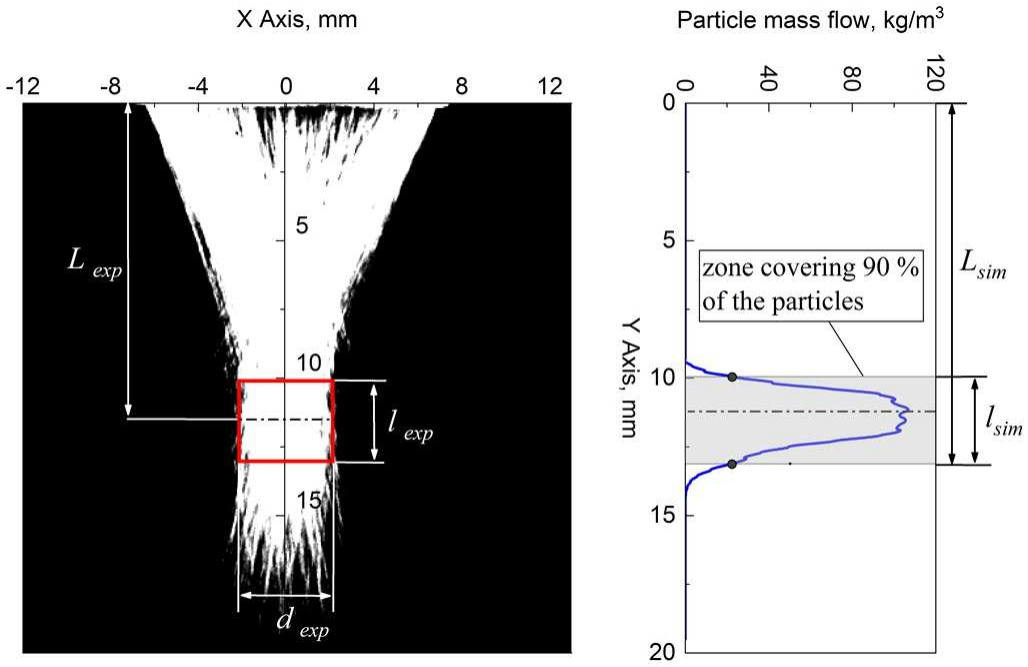

(a) (b)

Fig. 11. Comparison of the waist width/length obtained by the experiment (a) with the simulated one (b) for the "short" nozzle, gap is 0.5mm.

Comparison of the experimental and simulation results for the waist position and waist length is presented in Table 4.

Increase of the gap up-to 1 mm does not significantly affect the waist's width : for the "short" nozzle d = 3.9 ± 0,3 mm; for the "middle" nozzle d = 3,4 ± 0,3 mm.

The values of measured waist length, l, are well agreed with modelled one for coefficient α = 0.9 (Figure 11a).

The waist position obtained by simulation was defined as the maximum of particle masse flow along Y axis presented in the Figure 11b. It was supposed that the waist length is equal to the length of the zone covering 90% of the particles.

Table 4. Comparison of the experimental and simulation results for the waist position and waist length.

Nozzle type/ gap width, mm	Experimental waist position, *L,* mm	Simulated waist position, *L,* mm	Standoff distance, mm	Experimental waist length, *l*, mm	Simulated waist length, *l*, mm
Short, 0.5 mm	8.6±0.3	11.8±0.2	10.5-11.5	3.2±0.3	3.0±0.2
Short, 1.0 mm	9.3 ± 0.3	14.0±0.2	10.5-11.5	4.2±0.3	4.1±0.3
Medium, 0.5 mm	8.3±0.3	12.8±0.4	11.5-12.5	4.2±0.3	4.0±0.2
Medium, 1.0 mm	9.1 ± 0.3	14.8±0.3	11.5-12.5	4.9±0.3	5.3±0.4

The positions of maximum powder density zones do not coincide with the waist position (*L*) and length (*l*). This is due to the mutual-particles collisions and further jet focalization by coaxial gas flow.

5. Conclusions

The gas-powder flux in laser cladding was numerically and experimentally studied. The calculations were done for gas and powder movement applying Euler-Lagrange approximation and $k - \varepsilon$ turbulence model. Powder jet monitoring by high-speed camera was carried out for two types of Precitec cladding nozzles with different gaps. The co-called

"short" nozzle and the "medium" one were analysed with 0.5 and 1.0 mm gaps (see Figure 1 and Table 1). After post-treatment of the powder jet images, the simulation and experimental results were compared regarding the flow's convergence/divergence angles, waist geometry and position.

It was found that:

1. The convergence angle of the gas-powder flux depends on the nozzle's inclination angle and may be up to 32^{o} and 26^{o} for the "short" and "medium" nozzles, respectively. By increasing the gap width one increases the limit (maximal) convergence angle by about 10%.
2. By increasing the gap value, the maximum of the powder jet density is located at the maximal distance around 9 mm from the nozzle cut-off for both nozzles types. However, the density peak is higher in the case of the "short" nozzles.
3. Optical monitoring reveals the typical powder flux shape: It is converged with a certain angle and forms a waist. The "short" nozzles with the maximal gap width of 1.0 mm are characterised by more dense powder jet with the waist length of up to 4 mm.
4. The "medium" nozzles perform dense and more focalized powder jets, so they could be applied for direct 3D fabrication. The "short" nozzles are more suitable for deposition of protective coatings with wide cladding beads as well as for repairing operations. Since the convergence angle is higher for the "short" nozzles, their deposition efficiency is influenced in advance by powder jet defocalisation.
5. Simulation results have shown the same tendencies concerning the waist position and length, however the quantitative values are different: The measured waist length is close to the modelled one, especially, for the case of "short" nozzles without energy loses in particles/wall collisions. The influence of these collisions on simulation results is important.

6. Regarding the convergence\divergence angles: numerical results have shown the same tendency, however, the range of the calculated angles are typically less than the measured ones due to the absence of the particle-particle collisions in simulation.

6. Acknowledgment

The study was conducted with financial support from the Ministry of Science and Higher Education of the Russian Federation in the framework of Increase Competitiveness Program of NUST MISiS (K2-2019-009).

7. References

[1]. E. Toyserkani, A. Khajepour, S. F. Corbin, Laser Cladding, 1st edition, CRC Press, Boca Raton, 2004. https://doi:10.1201/9781420039177.

[2]. K. Partes, Analytical model of the catchment efficiency in high speed laser cladding, Surf. Coat. Technol. 204 (3) (2009) 366–371.

[3]. A. Zhang, D. Li, Z. Zhou, G. Zhu, B. Lu, Numerical simulation of powder flow field on coaxial powder nozzle in laser metal direct manufacturing, Int. J. Adv. Manuf. Technol. 49 (2010) 853 –859. https://doi: 10.1007/s00170-010-2657-8.

[4]. S. Zhou, X. Dai, H. Zheng, Analytical modeling and experimental investigation of laser induction hybrid rapid cladding for Ni based WC composite coatings, Opt. Laser Technol. 43(3) (2011) 613 – 621. https://doi:10.1016/j.optlastec.2010.09.001.

[5]. J. Lin, W. M. Steen, Design characteristics and development of a nozzle for coaxial laser cladding, J. Laser Appl. 10 (2011) 55. https://doi: 10.2351/1.521821.

[6]. J. Yan, I. Battiato, G. Fadel, Design of injection nozzle in direct metal deposition (DMD) manufacturing of thin-walled structures based on 3D models, Int. J. Adv. Manuf. Technol. 91 (2017) 605–616. https:// doi: 10.1007/s00170-016-9773-z.

[7]. M. Cortina, J.I. Arrizubieta, J.E. Ruiz, A. Lamikiz, E. Ukar, Design and manufacturing of a protective nozzle for highly reactive materials processing via Laser Material Deposition, Procedia CIRP 68 (2018) 387 – 392. https:// doi: 10.1016/j.procir.2017.12.100.

[8]. H. Ju, Z. J. Zhang, C. X. Lin, Z. J. Liu, H. L. Jiang, Design optimization and experimental study of coaxial powder-feeding nozzle in the laser cladding process, IOP Conference Series: Materials Science and Engineering, 474(1) (2019). https://doi.org/10.1088/1757-899X/474/1/012008.

[9]. H. Liu , X. L. He, G. Yu, Z. B. Wang, S. X. Li, C. Y. Zheng, W. J. Ning, Numerical simulation of powder transport behavior in laser cladding with coaxial powder feeding, Science China Physics, Mechanics & Astronomy. 58 (2015) 104701. https://doi.org/10.1007/s11433-015-5705-4.

[10]. Z. Liu, H. C. Zhang, S. Peng, H. Kim, D. Du, W. Cong, Analytical modeling and experimental validation of powder stream distribution during direct energy deposition. Addit. Manuf. 105 (2019) 4107–4121.

[11]. A. J. Pinkerton, Advances in the modeling of laser direct metal deposition, J. Laser Appl. 27 (S1) (2015) S15001. https://doi: 10.2351/1.4815992.

[12]. J. Lin, Numerical simulation of the focused powder streams in coaxial laser cladding. J. Mater. Process. Tech. 105(1–2) (2000) 17–23. https://doi:10.1016/S0924-0136(00)00584-7.

[13]. H. Pan, F. Liou, Numerical simulation of metallic powder flow in a coaxial nozzle for the laser aided deposition process, J. Mater. Process. Technol. 168 (2005) 230–244. https://doi: 10.1016/j.jmatprotec.2004.11.017.

[14]. O.B. Kovalev, I.O. Kovaleva, I.Y. Smurov, Numerical investigation of gas-disperse jet flows created by coaxial nozzles during the laser direct material deposition, J. Mater. Process. Technol. 249 (2017) 118-127. doi: 10.1016/j.jmatprotec.2017.05.041.

[15]. J-M. Jouvard, D. F. Grevey, F. Lemoine, A. B. Vannes, Continuous wave Nd: YAG laser cladding modeling: a physical study of track creation during lower power processing, J. Laser Appl. 9(1) (1997) 43–50. https://doi:10.2351/1.4745444.

[16]. P. Nie, O.A. Ojo, Z. Li, Modeling analysis of laser cladding of a nickel-based superalloy, Surf. Coat. Technol. 258 (2014) 1048-1059. https://doi: 10.1016/j.surfcoat.2014.07.030.

[17]. D. Eisenbarth, P. M. Borges Esteves, F. Wirth, K. Wegener, Spatial powder flow measurement and efficiency prediction for laser direct metal deposition, Surf. Coat. Technol. 362 (2019) 397–408. https://doi: 10.1016/j.surfcoat.2019.02.009.

[18]. B.A. Khamidullin, I.V. Tsivilskiy, A.I. Gorunov, A.Kh. Gilmutdinov, Modeling of the effect of powder parameters on laser cladding using coaxial nozzle, Surf. Coat. Tech. 364 (2019) 430–443. https://doi: 10.1016/j.surfcoat.2018.12.002.

[19]. J. Zhang, L. Yang, W. Zhang, J. Qiu, H. Xiao, Y. Liu, (2020), Numerical simulation and experimental study for aerodynamic characteristics and powder transport behavior of novel nozzle, Opt. Laser Eng. 126 (2020) 105873. https://doi: 10.1016/j.optlaseng.2019.105873.

[20]. M. Doubenskaia, D. Novichenko, A. Sova, D. Pervoushin, Particle-in-flight monitoring in thermal spray processes, Surf. Coat. Technol. 205 (2010) 1092–1095. https://doi: 10.1016/j.surfcoat.2010.07.075.

[21]. J. Lin, Concentration mode of the powder stream in coaxial laser cladding, Optics Laser Technol. 31 (1999) 251-257. https://doi.org/10.1016/S0030-3992(99)00049-3.

[22]. A. J. Pinkerton, L. Li, Modelling Powder Concentration Distribution From a Coaxial Deposition Nozzle for Laser-Based Rapid Tooling, J. Manuf. Sci. and Engin. 126 (1) (2004) 33-41. https://doi: 10.1115/1.1643748.

[23]. E. Ferreira, M. Dal, Ch. Colin, G. Marion, C. Gorny, D. Courapied, J. Guy, P. Peyre, Experimental and Numerical Analysis of Gas/Powder Flow for Different LMD Nozzles, Metals 10(5) (2020) 667. https://doi: 10.3390/met10050667.

[24]. S. Zekovic, R. Dwivedi, R. Kovacevic, Numerical simulation and experimental investigation of gas-powder flow from radially symmetrical nozzles in laser-based direct metal deposition, Int. J. Mach. Tools Manuf. 47 (2007) 112–113. https://doi:10.1016/j.ijmachtools.2006.02.004.

[25]. H. Tan, F. Zhang, R. Wen, J. Chen, W. Huang, Experiment study of powder flow feed behavior of laser solid forming. Optics Lasers Engin. 50 (3) (2012) 391–398. https://doi:10.1016/j.optlaseng.2011.10.017.

[26]. H. Tan, C. Zhang, W. Fan, F. Zhang, X. Lin, J. Chen, W. Huang, Dynamic evolution of powder stream convergence with powder feeding durations in direct energy deposition, Int. J. Mach. Tool Manu. 157 (2020) 103606. https:// doi.org/10.1016/j.ijmachtools.2020.103606.

[27]. P. Balu, P. Leggett, R. Kovacevic, Parametric study on a coaxial multi-material powder flow in laser-based powder deposition process, J. Mater. Process. Tech. 212(7) (2012) 1598–1610, https://doi:10.1016/j.jmatprotec.2012.02.020.

[28]. I. Tabernero, A. Lamikiz, E. Ukar, L. N. López de Lacalle, C. Angulo, G. Urbikain, Numerical simulation and experimental validation of powder flux distribution in coaxial laser cladding, J. Mater. Process. Technol. 210 (2010) 2125–2134. https://doi: 10.1016/j.jmatprotec.2010.07.036.

[29]. S. Y. Wen, Y. C. Shin, J. Y. Murthy, P. E. Sojka, Modeling of coaxial powder flow for the laser direct deposition process, Int. J. Heat. Mass. Transf. 52 (25-26) (2009) 5867–5877. https://doi:10.1016/j.ijheatmasstransfer.2009.07.018.

[30]. P. Fauchais, A. Vardelle, M. Vardelle, Modelling of Plasma Spraying of Ceramic Coatings at Atmospheric Pressure, Ceram. Int. 17 (1991) 367-378.

[31]. Precitec laser cladding, Laser deposition welding with metal powder - focusing optics YC30, https://www.precitec.com/laser-welding/products/processing-heads/yc30/, 2020 (accessed 30 August 2020).

[32]. S. Nowotny, S. Scharek, E. Beyer, K. H. Richter, Laser beam build-up welding: Precision in repair, surface cladding, and direct 3d metal de-position, J. Therm. Spray Tech. 16 (2007) 344–348. https://doi:10.1007/s11666-007-9028-5.

[33]. Yu. M. Tsirkunov, S. V. Panfilov, M. B. Klychnikov, M.B., Semiempirical model of impact interaction of a disperse impurity particle with a surface in a gas suspension flow, J. Eng. Phys. Thermophys. 67 (1994) 1018–1025.

[34]. O.B. Kovalev, A.V. Zaitsev, D. Novichenko, I. Smurov, Theoretical and Experimental Investigation of Gas Flows, Powder Transport and Heating in Coaxial Laser Direct Metal Deposition (DMD) Process, J. Therm. Spray Tech. 20(3) (2011) 465478. https://doi.org/10.1007/s11666-010-9539-3.

Appendix

Nomenclature	
k	Turbulent kinetic energy
ε	Turbulent energy dissipation
ρ	Gas density
u_i	Velocity
x_i	Position
E_{ij}	Component of rate of deformation
μ_T	Eddy (turbulent) viscosity
Pr_t	Turbulent Prandtl number
G_k	Generation of turbulence kinetic energy due to the velocity gradients
G_b	Generation of turbulence kinetic energy due to the buoyancy
g	Gravitational acceleration
m_p	Mass of the particle
V_p	Volume of the particle
a_p	Acceleration of the particle
F_i	Acting force
u_p	Velocity of the particle
u	Velocity of the fluid phase
t	Time
d_p	Diameter of the particle
R_e	Reynolds number
φ	Shape factor
C_d	Drag coefficient
T	Temperature

P	Pressure
S	Surface area of the particle
s	Surface area of the sphere
α	Loses coefficient
M	Mach number
d	Width of the waist
l	Length of the waist
L	Position of the waist
θ_{convm}	Main convergence angle
θ_{conv1}	First limit angle
θ_{conv2}	Second limit angle
θ_{divl}	Divergence angle